Article

Journal of Advanced Electrochemical Storage

www.pubj.org

Solvent-Engineered Synthesis of V_2O_5 for Enhanced Supercapacitor Performance

Tholkappiyan Ramachandran[1,2,*], Santhoshkumar Palanisamy[3], Ramesh Kumar Raji[4]

[1]Saveetha School of Engineering, Saveetha Institute of Medical and Technical Sciences, Saveetha University, Chennai 602105, Tamil Nadu, India.
[2]Department of Physics, Khalifa University of Science and Technology, Abu Dhabi, P. O. Box 127788, United Arab Emirates. E-mail: tholkappiyan.ramachandran@ku.ac. ae
[3]Department of Mechanical and Nuclear Engineering, Khalifa University of Science and Technology, 127788, Abu Dhabi, United Arab Emirates.
[4]Department of Physics, College of Science, United Arab Emirates University, Al-Ain, Abu Dhabi, P. O. Box 15551, United Arab Emirates.

Cite This: *J. Adv. Electro. Storage* 2025, 1, 1–20

ABSTRACT: Vanadium pentoxide (V_2O_5) is considered a promising electrode material for supercapacitors due to its rich redox chemistry, high theoretical capacitance, and layered structure conducive to ion intercalation. However, its practical performance is often limited by poor electrical conductivity and structural instability during cycling. In this study, a series of vanadium pentoxide (V_2O_5)-based electrode materials were synthesized via a solvothermal route by varying the ratio of isopropyl alcohol (IPA), glycerol, and deionized (DI) water to investigate their influence on structural, morphological, and electrochemical properties for supercapacitor applications. X-ray diffraction (XRD) confirmed the orthorhombic phase of V_2O_5 in all samples, while UV–Vis spectroscopy showed solvent-driven modulation of optical bandgaps, indicating altered electronic structures. X-ray photoelectron spectroscopy (XPS) revealed mixed-valence vanadium states and oxygen vacancies, particularly in glycerol-rich samples. Surface morphology examined through scanning electron microscopy (SEM) revealed solvent-dependent architectures from compact aggregates in water-only samples to highly porous, flower-like assemblies in mixed solvent systems. Notably, Sample 3, prepared with 40:20:10 mL of IPA, glycerol, and DI water, exhibited a 3D nanosheet-based morphology, confirmed by transmission electron microscopy (TEM), which enhances ion accessibility and shortens diffusion pathways. Energy-dispersive X-ray spectroscopy (EDS) elemental mapping verified the homogeneous distribution of V and O elements across all samples, confirming compositional consistency. Electrochemical studies, including cyclic voltammetry (CV), galvanostatic charge–discharge (GCD), and electrochemical impedance spectroscopy (EIS), demonstrated that Sample 3 delivered the highest specific capacitance (~104 F g^{-1}), excellent redox reversibility, and low charge-transfer resistance. These results highlight the critical role of solvent engineering in tuning the morphology and electrochemical performance of V_2O_5-based electrodes, making them promising candidates for high-efficiency supercapacitors.

1. INTRODUCTION

The global transition towards renewable energy and the proliferation of portable electronics and electric vehicles have necessitated the development of next-generation energy storage technologies [1-3]. Supercapacitors, often referred to as electrochemical capacitors, have emerged as a powerful complement to conventional batteries

due to their ability to provide high power density, rapid charge/discharge capability, and excellent cycle stability [4]. These attributes make them highly suitable for applications requiring instantaneous energy delivery, such as regenerative braking systems, uninterruptible power supplies, and hybrid energy systems. However, the limited energy density of supercapacitors remains a major bottleneck. Improving this aspect requires strategic development of electrode materials with high specific capacitance and favorable electrochemical kinetics [5]. Transition metal oxides, with their rich redox activity and pseudocapacitive nature, offer a pathway to significantly enhance the energy density of supercapacitor systems [6]. Vanadium pentoxide (V_2O_5) is one such transition metal oxide that has garnered considerable interest in energy storage research. Its layered orthorhombic structure facilitates intercalation/de-intercalation of electrolyte ions, enabling fast redox reactions and high theoretical specific capacitance [7]. Moreover, V_2O_5 is abundant, cost-effective, and environmentally benign, further elevating its potential as a high-performance supercapacitor electrode material. Despite these advantages, V_2O_5 suffers from several intrinsic limitations, such as poor electrical conductivity, structural degradation during prolonged cycling, and sluggish ion diffusion [8]. These challenges limit its practical applicability and necessitate innovative strategies to modulate its structural, morphological, and electrochemical properties. Tailoring the morphology and crystallinity of V_2O_5 through precise synthetic control has emerged as a promising approach to overcoming these drawbacks and enhancing its electrochemical performance [9].

Solvothermal synthesis has been recognized as an effective route for fabricating nanostructured materials with tunable physical and chemical characteristics. This method, carried out in a sealed autoclave under controlled temperature and pressure, allows for the growth of highly crystalline and morphologically diverse nanostructures [10]. Among the various parameters that influence solvothermal synthesis, the composition of the solvent system plays a pivotal role in governing the nucleation rate, crystal growth mechanism, and final morphology of the resulting product. The solvent environment directly impacts the solubility of precursors, the dielectric constant of the medium, and the extent of hydrolysis and condensation reactions. Hence, by systematically varying the solvent composition, it becomes possible to manipulate the microstructural evolution and optimize the physicochemical properties of V_2O_5 for enhanced capacitive behavior [11]. Alcohols and polyols have shown great promise as co-solvents in solvothermal systems due to their ability to influence particle size, morphology, and dispersion of metal oxides. Isopropyl alcohol (IPA), being a protic solvent with moderate polarity, can serve as a structure-directing agent and promote uniform particle dispersion. On the other hand, glycerol, a viscous polyol with multiple hydroxyl groups, acts as a chelating agent and a stabilizer during the growth of metal oxides [12]. The synergistic interaction of IPA and glycerol with water creates a complex solvation environment that

alters the crystallization kinetics of vanadium species. Higher glycerol content can potentially promote the formation of more interconnected, porous structures, while IPA can accelerate nucleation and improve particle uniformity. The interplay between these solvents significantly determines the final microstructure, porosity, and electrochemical accessibility of the active material [13].

In light of this, the present study is centered on synthesizing a series of V_2O_5 nanostructures using a solvothermal technique by varying the composition of the solvent mixture. Four different samples were synthesized under identical thermal and precursor conditions, with only the solvent ratios being systematically altered. Sample 1 was prepared using deionized (DI) water as the sole solvent, serving as a reference. Sample 2 used a mixture of 50 mL IPA, 10 mL glycerol, and 10 mL DI water; Sample 3 involved 40 mL IPA, 20 mL glycerol, and 10 mL DI water; while Sample 4 was synthesized with 30 mL IPA, 30 mL glycerol, and 10 mL DI water. This gradient in solvent composition was designed to probe the influence of increasing glycerol content and decreasing IPA proportion on the nucleation behavior, morphology, and eventual electrochemical performance of the synthesized V_2O_5 structures. All samples were subjected to identical post-synthesis treatment including washing, drying, and grinding to maintain consistency in characterization.

Comprehensive physicochemical and electrochemical characterizations were carried out on the synthesized V_2O_5 samples. Structural analysis using X-ray diffraction (XRD) was performed to confirm the phase purity and crystallinity of each sample, while scanning electron microscopy (SEM) and transmission electron microscopy (TEM) provided insight into the morphological variations induced by solvent composition. Elemental mapping and energy-dispersive X-ray spectroscopy (EDX) were employed to confirm the uniform distribution of vanadium and oxygen. Furthermore, surface chemical states were examined using X-ray photoelectron spectroscopy (XPS), and specific surface area measurements were conducted via Brunauer-Emmett-Teller (BET) analysis. These results were correlated with electrochemical performance metrics such as cyclic voltammetry (CV), galvanostatic charge-discharge (GCD), and electrochemical impedance spectroscopy (EIS), obtained from three-electrode cell configurations using 2 M H_2SO_4 electrolyte.

The principal aim of this research is to systematically investigate how the variation in IPA and glycerol concentrations within the solvent system influences the structural evolution, morphological characteristics, and electrochemical behavior of solvothermally synthesized V_2O_5 nanostructures. By establishing a clear relationship between solvent composition and material performance, this work seeks to provide a rational design strategy for optimizing V_2O_5-based electrode materials. The findings are expected to advance our understanding of solvent-directed synthesis and facilitate the development of high-efficiency pseudocapacitive materials for next-generation energy storage devices.

2. Experimental

2.1. Synthesis of Electrode Samples via Solvothermal Method

Four vanadium pentoxide (V_2O_5)-based electrode samples were synthesized using a controlled solvothermal process to investigate the effect of solvent composition on the electrochemical performance of supercapacitor electrodes. The solvothermal reactions were carried out in a Teflon-lined stainless steel autoclave at 180° C for 12 hours. Analytical grade reagents were used without further purification.

Sample 1 (Bare V_2O_5):

For the baseline sample, 0.5 g of V_2O_5 powder was dispersed in 70 mL of deionized (DI) water under magnetic stirring for 30 minutes to form a uniform suspension. The solution was then transferred into the autoclave and maintained at the reaction temperature. After cooling to room temperature, the resulting product was washed several times with DI water and ethanol, and then dried at 60° C for 12 hours.

Sample 2 (V_2O_5 with IPA/Glycerol/DI Water – 50:10:10 mL):

In this sample, 0.5 g of V_2O_5 was added to a mixed solvent system containing 50 mL isopropyl alcohol (IPA), 10 mL glycerol, and 10 mL DI water. The mixture was stirred vigorously for 30 minutes to ensure homogeneity. The suspension was transferred into the autoclave and subjected to solvothermal treatment. Post-treatment, the sample was washed thoroughly and dried as described for Sample 1.

Sample 3 (V_2O_5 with IPA/Glycerol/DI Water – 40:20:10 mL):

The synthesis procedure was similar to Sample 2, with the solvent composition adjusted to 40 mL IPA, 20 mL glycerol, and 10 mL DI water. After stirring and autoclaving, the product was collected, washed, and dried under the same conditions.

Sample 4 (V_2O_5 with IPA/Glycerol/DI Water – 30:30:10 mL):

For this variant, the solvent mixture consisted of 30 mL IPA, 30 mL glycerol, and 10 mL DI water. The V_2O_5 precursor (0.5 g) was dispersed in the solvent, stirred for 30 minutes, and then subjected to the solvothermal process. The final product was washed and dried as per the aforementioned protocol. All the synthesized samples were ground into fine powders and stored in airtight containers for further characterization and electrode fabrication.

2.2 Electrode Material Characterization of Samples 1 to 4

The structural, morphological, and compositional characteristics of the synthesized electrode materials (Samples 1 to 4) were comprehensively analyzed to evaluate their suitability for energy storage applications. X-ray diffraction (XRD) analysis was performed using a Rigaku D/max-RB diffractometer equipped with Cu Kα radiation (λ = 0.15406 nm) to identify the crystalline phases and assess the structural integrity of each sample. The obtained diffraction patterns were matched with standard reference data to confirm phase purity and successful incorporation of metallic and oxide constituents. Key parameters such as peak position, intensity, and full width at half maximum (FWHM) were examined to assess

crystallinity and detect any secondary phases. The comparisons among the samples highlighted variations in crystalline quality resulting from different synthesis protocols. To further investigate the morphology and surface texture, scanning electron microscopy (SEM) was employed using a Hitachi S4800 (Japan) microscope. SEM images revealed distinct structural features across Samples 1 to 4, including differences in particle shape, surface roughness, and agglomeration tendencies. Elemental mapping through energy-dispersive X-ray spectroscopy (EDS) attached to the SEM confirmed the uniform distribution of key elements across all samples. This homogeneity is essential for achieving stable electrochemical behavior. The microstructural comparison also helped assess porosity and interconnectivity, which are important for enhancing ion transport and charge storage.

High-resolution insights into the nanostructure and interfacial coherence were obtained via transmission electron microscopy (TEM) using a Tecnai G2F20 system (Germany). TEM and high-resolution TEM (HRTEM) images revealed lattice fringes indicative of high crystallinity and good structural ordering in all four samples, though with varying degrees of uniformity and defect density. Selected area electron diffraction (SAED) patterns confirmed the polycrystalline nature and phase composition. In addition, elemental mapping using EDS integrated with TEM provided spatial distribution of elements, validating the compositional uniformity at the nanoscale across each sample. X-ray photoelectron spectroscopy (XPS) analysis was conducted using a Thermo K-alpha+ spectrometer with an Mg Kα excitation source to explore the surface chemical composition and oxidation states of the constituent elements. The deconvoluted high-resolution spectra of Zn 2p, Mn 2p, Ni 2p, and O 1s enabled identification of the respective oxidation states and electronic environments, revealing differences in surface chemistry among Samples 1 to 4. These differences are expected to influence redox activity and overall electrochemical behavior.

2.3 Fabrication of Electrodes Using Samples 1–4

To prepare the working electrodes for electrochemical analysis, a uniform protocol was followed for all four samples (Sample 1 to Sample 4). Nickel plates (1 cm × 1 cm) were employed as the current collectors. Prior to material deposition, the plates underwent a thorough cleaning procedure to remove surface oxides and contaminants. Each nickel plate was immersed in a 3 M HCl solution and ultrasonicated for 30 minutes. Subsequently, the plates were rinsed sequentially with deionized water, ethanol, and acetone to ensure surface purity, then dried at 80° C for 10 hours in a hot air oven to remove any residual solvents and moisture. The electrode slurries for each sample were prepared by mixing the synthesized materials (Sample 1 to Sample 4) with activated carbon and polyvinylidene fluoride (PVDF) in a weight ratio of 8:1:1. Activated carbon was used to enhance electrical conductivity, while PVDF served as a binder to ensure mechanical cohesion. A few drops of 1-methyl-2-pyrrolidinone (NMP) were added to improve the viscosity and uniformity of the slurry. The resulting pastes were then carefully applied to the cleaned nickel plates

via a drop-casting method, forming coatings with an approximate thickness of 0.5 mm. After air drying, the electrodes were subjected to thermal treatment at 100° C for 8 hours to achieve strong adhesion and complete solvent evaporation. The final mass of the active material on each electrode was controlled within the range of 0.3 to 0.5 mg to ensure consistency in electrochemical testing.

Electrochemical evaluations were carried out at room temperature using a standard three-electrode system connected to a SP-Bio-Logical electrochemical workstation [14]. The synthesized material-coated nickel plates (Samples 1 to 4) served as the working electrodes. A platinum foil and a saturated Ag/AgCl electrode were employed as the counter and reference electrodes, respectively. A 2 M H_2SO_4 aqueous solution was used as the electrolyte to facilitate efficient proton conduction and ion exchange. Cyclic voltammetry (CV) tests were performed over a potential range of 0 to 0.6 V at varying scan rates to investigate the charge storage behavior of each sample. Galvanostatic charge-discharge (GCD) measurements were conducted within a voltage window of 0 to 0.5 V to assess the specific capacitance and rate capability of the electrodes. Electrochemical impedance spectroscopy (EIS) measurements were also performed over a frequency range of 0 to 200 Hz with a 5 mV AC signal to evaluate the charge transfer resistance and ionic diffusion characteristics. The specific capacitance (C_e, F g^{-1}) for each sample was calculated from the GCD curves using the following equation [15]:

$$C_e = I(\Delta t) / m(\Delta V) \quad (1)$$

where I is the discharge current (A), Δt is the discharge time (s), m is the mass of active material (g), and ΔV is the applied voltage window (V). This uniform fabrication and testing protocol enables a reliable comparison of the electrochemical properties of Samples 1 to 4. Variations in performance can be attributed to the differences in material morphology, crystallinity, and composition derived from the specific synthesis conditions. The comparative analysis of these samples will provide insights into optimizing material design for high-performance supercapacitor electrodes.

3. Results and discussion

3.1. Structural and Optical Characterization

X-ray Diffraction (XRD) Analysis

Figure 2(a) presents the XRD patterns of the synthesized vanadium pentoxide (V_2O_5)-based electrode samples. The diffraction peaks observed for Sample 1 (Bare V_2O_5) match well with the orthorhombic phase of V_2O_5 (JCPDS Card No. 41-1426), confirming the successful formation of crystalline V_2O_5 [16]. With the incorporation of different ratios of isopropyl alcohol (IPA), glycerol, and DI water in Samples 2 to 4, a noticeable variation in peak intensity and slight broadening are observed. This indicates a change in crystallinity and possible reduction in grain size due to solvent-mediated morphological tuning during the solvothermal

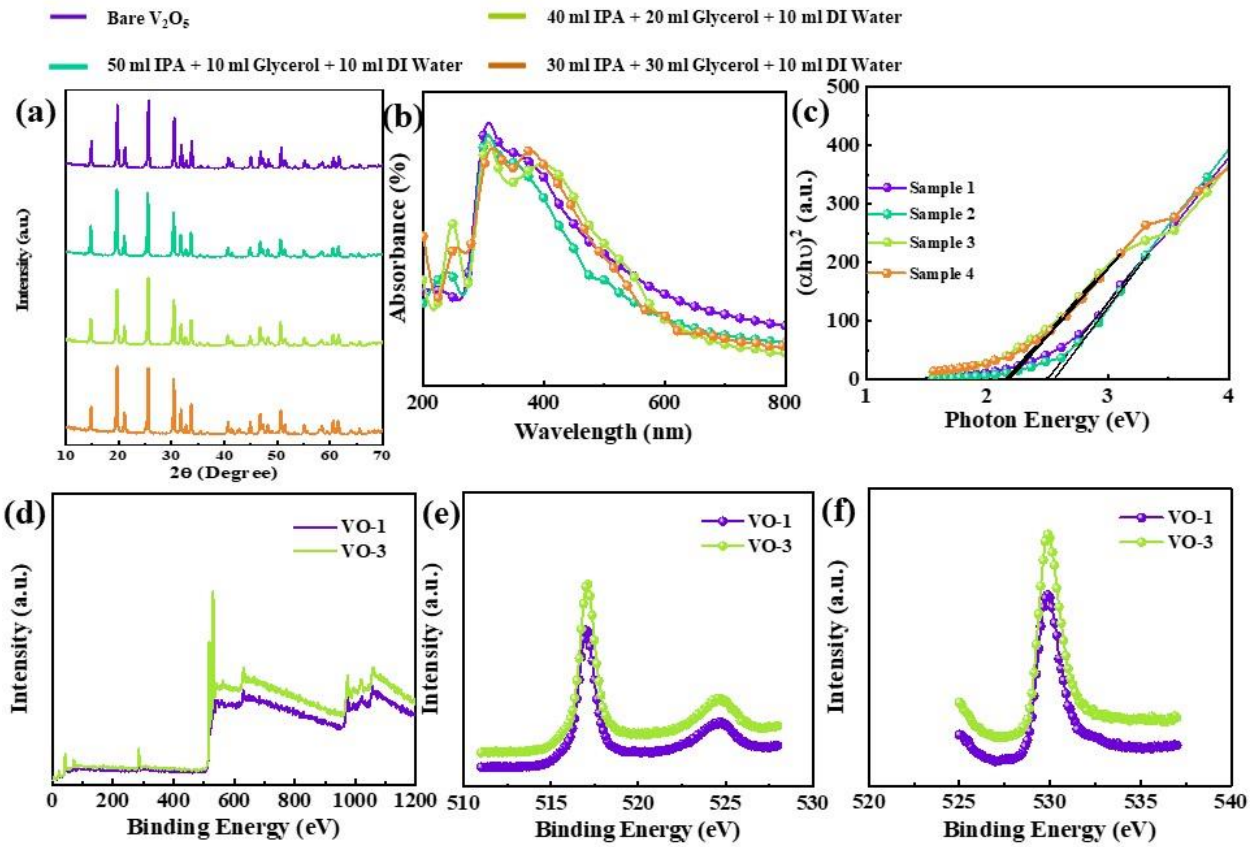

synthesis [17]. Sample 4, with the highest glycerol content, shows the most significant broadening, suggesting smaller crystallites or increased amorphization, which could potentially enhance electrochemical activity due to improved ion diffusion pathways.

UV-Visible Absorption Spectroscopy

Figure 2(b) displays the UV-Vis absorbance spectra of all samples, showing strong absorption in the UV to visible region (200–800 nm). All samples exhibit characteristic V_2O_5 absorption bands due to ligand-to-metal charge transfer transitions. Compared to Bare V_2O_5, the modified samples show slight redshifts and increased absorbance in the visible region, implying improved light-harvesting properties. Figure 2(c) shows the Tauc plots derived from the absorbance data, used to estimate the optical bandgap. The bandgap values are found to be in the range of 2.3–2.7 eV. A gradual decrease in bandgap is observed from Sample 1 to Sample 4, attributed to the increased glycerol content, which may introduce defect states or enhance electron delocalization, thus improving electronic conductivity an important trait for supercapacitor applications [18].

X-ray Photoelectron Spectroscopy (XPS)

Figure 2. (a) XRD patterns of Bare V_2O_5 (Sample 1), and solvothermally synthesized V_2O_5 in different IPA/glycerol/DI water ratios (Samples 2–4); (b) UV-Visible absorbance spectra; (c) Tauc plots for bandgap estimation; (d) XPS full survey spectra for VO-1 (Sample 1) and VO-3 (Sample 3); (e) High-resolution XPS

spectra of V 2p region; (f) High-resolution XPS spectra of O 1s region.

To further understand the chemical states and surface composition, XPS analysis was conducted, as shown in Figures 2(d–f). The full survey spectra (Figure 2(d)) confirm the presence of vanadium and oxygen without any noticeable impurities. High-resolution V 2p spectra (Figure 2(e)) exhibit two main peaks corresponding to V $2p_{3/2}$ and V $2p_{1/2}$, centered around 517.4 eV and 524.8 eV, respectively, indicating the presence of V^{5+} species. However, a slight shoulder in Sample VO-3 (Sample 3) suggests the presence of V^{4+} states, pointing toward partial reduction induced by the solvothermal environment and glycerol's mild reducing nature [19]. The O 1s spectra (Figure 2(f)) further support this, with peaks near 530.5 eV corresponding to lattice oxygen and a secondary component at higher binding energies related to adsorbed hydroxyl groups or water molecules [19]. Sample VO-3 exhibits a more pronounced shoulder, indicating increased surface hydroxylation, which could enhance electrolyte accessibility and pseudo-capacitive behavior [20]. These findings collectively reveal that solvent composition significantly influences the structural, optical, and electronic properties of V_2O_5 materials. In particular, increased glycerol content (Sample 3 and 4) promotes defect-rich, nanostructured surfaces with reduced bandgap and favorable surface chemistry, making them promising candidates for enhanced electrochemical performance in supercapacitor applications [21].

3.2. Morphology Characterization

The surface morphology of the synthesized V_2O_5-based electrode materials was examined using scanning electron microscopy (SEM), as shown in Figure 3. Each sample's microstructure reflects the effect of solvent composition on particle growth, assembly, and porosity, which are crucial for electrochemical performance in supercapacitor applications. Sample 1 (Figure 3a–a2), synthesized using only deionized water, shows aggregated particles forming quasi-spherical clusters with relatively smooth and compact surfaces [22]. The absence of porosity and the dense packing suggest limited ion accessibility and lower effective surface area, which could hinder electrochemical performance. In contrast, Sample 2 (Figure 3b–b2), prepared with a mixture of isopropyl alcohol (IPA), glycerol, and DI water (50:10:10 mL), displays a more uniform spherical morphology with roughened textures and partially developed porosity. The presence of IPA facilitates better dispersion and self-assembly, resulting in improved structural features that are favorable for ion diffusion and charge storage [23]. Sample 3 (Figure 3c–c2), obtained using a 40:20:10 mL solvent ratio, exhibits a well-defined 3D flower-like or dandelion-shaped architecture composed of interconnected nanosheets. This highly porous and hierarchical structure significantly enhances the accessible surface area and shortens ion diffusion paths, making it ideal for high-rate supercapacitor applications [24]. With further increase in glycerol content (30:30:10 mL), Sample 4 (Figure 3d–d2) shows densely

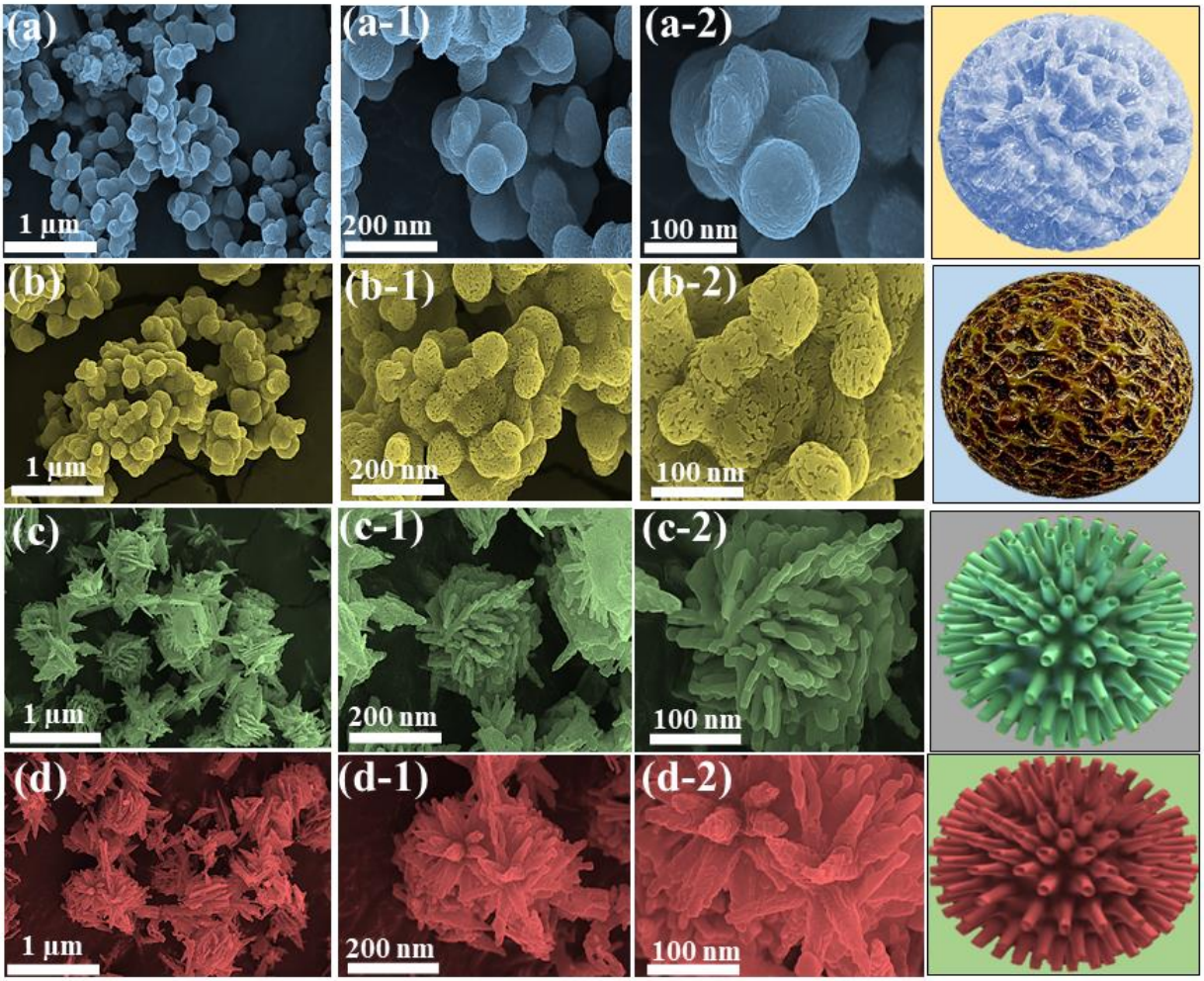

entangled nanosheets forming a spike-ball-like morphology. Although the architecture remains 3D and robust, the excessive viscosity from glycerol may lead to sheet thickening and partial blocking of ion channels, possibly affecting rate capability despite improved cycling stability [25]. Overall, the SEM analysis confirms that tuning the IPA/glycerol ratio during solvothermal synthesis plays a vital role in tailoring the microstructure of V_2O_5 electrodes. Among the samples, Sample 3 exhibits the most optimal morphology for high-performance supercapacitor electrodes, balancing porosity, surface area, and structural integrity [26].

Figure 3. SEM images of V_2O_5 samples synthesized via solvothermal method with varying solvent compositions: (a–a2) Sample 1 (DI water only), (b–b2) Sample 2 (IPA/Glycerol/DI = 50:10:10 mL), (c–c2) Sample 3 (IPA/Glycerol/DI = 40:20:10 mL), and (d–d2) Sample 4 (IPA/Glycerol/DI = 30:30:10 mL). Rightmost column shows corresponding schematic representations of the particle morphologies.

The elemental distribution and composition of the synthesized V_2O_5 samples were investigated using SEM-based energy-dispersive X-ray spectroscopy (EDS) and elemental mapping, as presented in Figure 4.

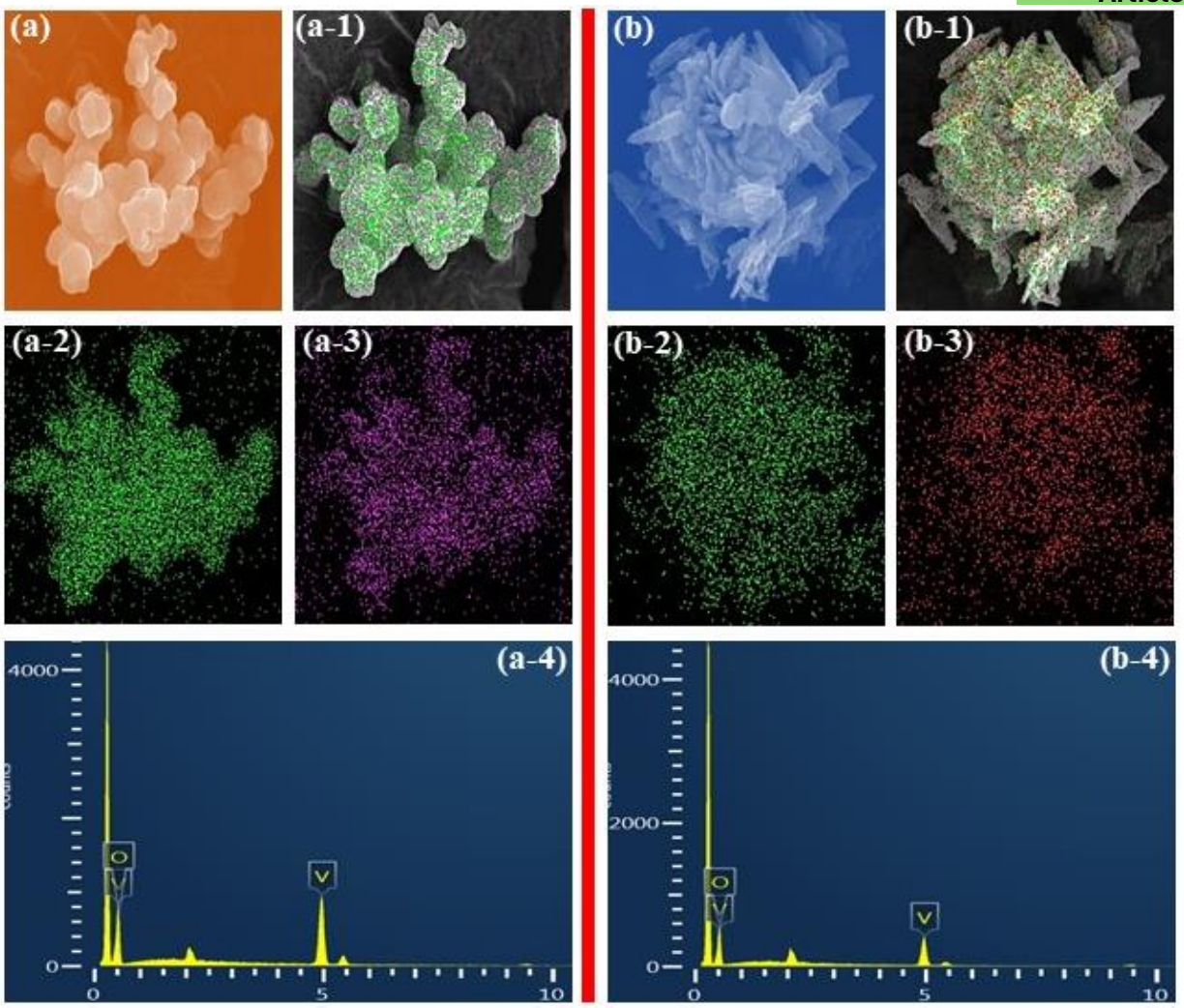

These analyses confirm the uniformity of vanadium (V) and oxygen (O) distribution and the purity of the synthesized materials. Sample 1, shown in Figures 4a–a4, exhibits a particle-like morphology with a relatively smooth surface, consistent with earlier SEM observations. The EDS mapping images (Figures 4a-2 and 3a-3) clearly indicate a homogeneous distribution of vanadium (green) and oxygen (magenta) across the sample. The corresponding EDX spectrum (Figure 4a-4) confirms the elemental presence of vanadium and oxygen with no detectable impurity peaks, indicating the successful formation of V_2O_5 without secondary phases. The sharp and distinct peaks for V and O also validate the high purity of the synthesized product. In contrast, Sample 3 (Figures 4b–b4) displays a distinctly different morphology composed of interconnected nanosheets. The EDS elemental mapping images (Figures 4b-2 and 4b-3) again confirm the uniform spatial distribution of vanadium (green) and oxygen (red), without any noticeable clustering or elemental segregation. This even distribution is crucial for consistent electrochemical behavior across the electrode. The EDX spectrum (Figure 4b-4) mirrors that of Sample 1, showing only vanadium and oxygen peaks, further confirming the material purity and the absence

of residual precursors or byproducts introduced during solvothermal synthesis. Overall, both samples demonstrate high elemental purity and homogeneity. However, the refined nanostructure and hierarchical morphology of Sample 3, combined with its uniform elemental distribution, suggest superior electrochemical performance due to enhanced surface reactivity and better electrolyte accessibility [27].

Figure 4. SEM images, elemental mapping, and EDX spectra of (a–a4) Sample 1 (Bare V_2O_5) and (b–b4) Sample 3 (V_2O_5 synthesized with IPA/Glycerol/DI = 40:20:10 mL). Panels a-1 and b-1 show the overlaid mapping; a-2/b-2 and a-3/b-3 represent vanadium and oxygen distribution, respectively; a-4 and b-4 show the corresponding EDX spectra.

Transmission electron microscopy (TEM) coupled with SAED, high-resolution imaging, and line-scan elemental analysis was employed to further elucidate the structural features and compositional uniformity of the synthesized samples. The results are depicted in **Figure 5**. Figures 5a–a3 illustrate the TEM characterization of Sample 1. The low-magnification TEM image (Figure 5a) reveals large, thin sheet-like structures with slightly curved edges, characteristic of aggregated V_2O_5 nanoplates. The higher magnification image (Figure 5a-1) displays well-defined lamellar layers, indicating a moderately ordered arrangement. The SAED pattern (Figure 5a-2) shows distinct and sharp diffraction spots arranged in concentric rings, confirming the polycrystalline nature of the material. The HRTEM image (Figure 5a-3) further reveals visible lattice fringes with a d-spacing of approximately 0.34 nm, corresponding to the (110) plane of orthorhombic V_2O_5. This crystallographic integrity supports the formation of phase-pure V_2O_5 with moderate crystallinity. In contrast, Sample 3 exhibits a more compact and denser nanoparticle morphology as shown in Figures 5b–b3. The TEM images (Figures 5b and 5b-1) reveal aggregated spherical particles composed of ultrathin nanosheets, which enhance the structural complexity and surface accessibility. The HRTEM image (Figure 5b-2) displays continuous and well-resolved lattice fringes, confirming high crystallinity. The SAED pattern (Figure 5b-3) also shows distinct diffraction rings with brighter intensity compared to Sample 1, further confirming improved crystallinity and better orientation of crystal planes. The line-scan elemental analysis profiles (Figures 5c and 5d) complement the morphological findings. For Sample 1 (Figure 5c), the vanadium (green) and oxygen (red) intensities are uniformly distributed along the scanned region, indicating homogenous elemental distribution without significant phase segregation. In Sample 3 (Figure 5d), the elemental profiles also demonstrate a consistent distribution of vanadium and oxygen, but with slightly higher signal intensity and sharper peak separation, suggesting a more densely packed structure and possibly a higher degree of oxidation. These observations indicate that the solvent composition in Sample 3 promotes better crystalline growth, structural compactness, and uniform elemental distribution, which are favorable for efficient charge transport and enhanced

electrochemical performance in supercapacitor applications [28].

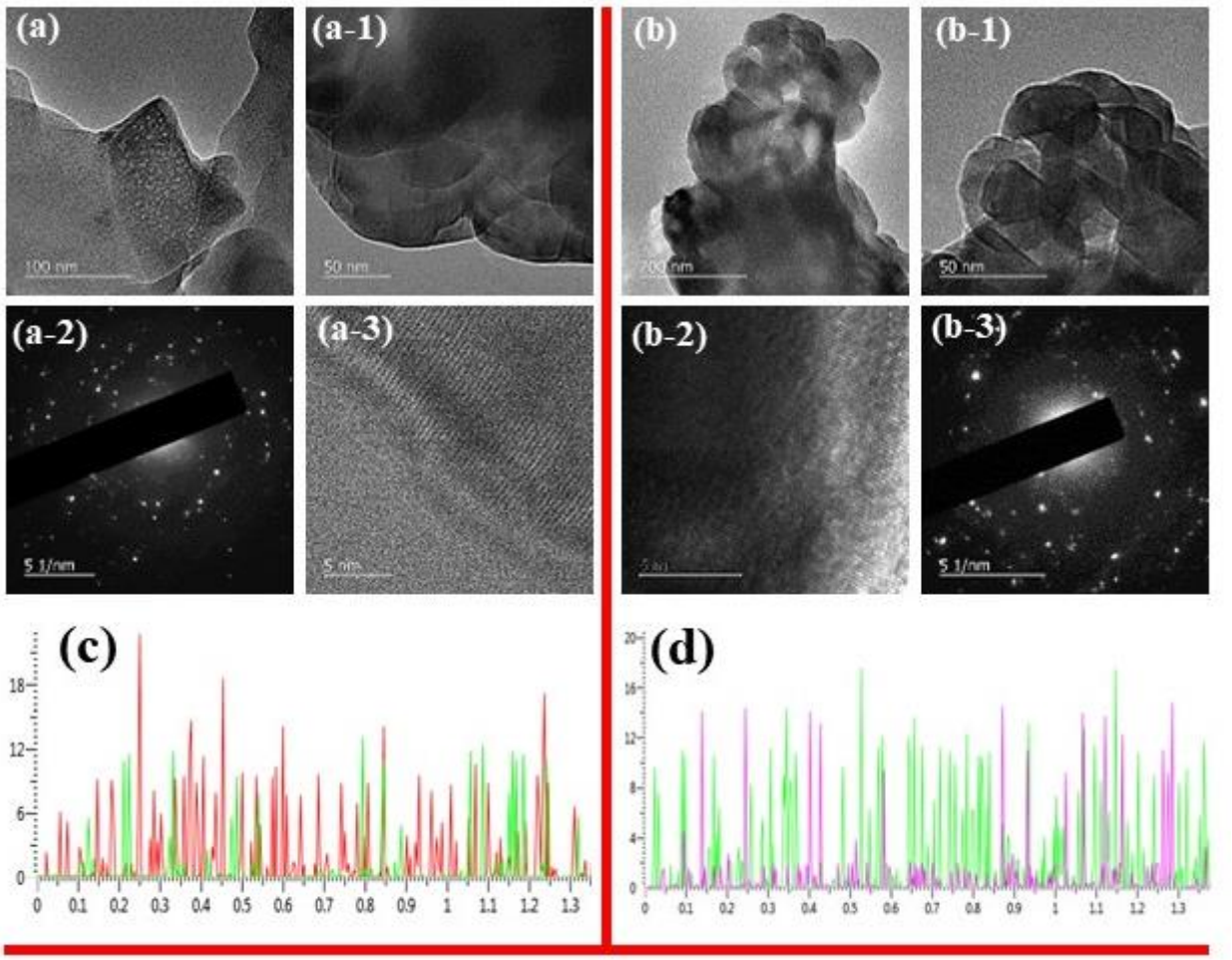

Figure 5. TEM analysis and line-scan mapping of (a–a3, c) Sample 1 (Bare V_2O_5) and (b–b3, d) Sample 3 (V_2O_5 with IPA/Glycerol/DI = 40:20:10 mL). (a, b) show low-magnification TEM images; (a-1, b-1) show higher magnification morphologies; (a-2, b-3) present SAED patterns; (a-3, b-2) display HRTEM images with visible lattice fringes; (c, d) represent the line-scan elemental distributions of vanadium and oxygen across the samples.

3.3. Electrochemical Validation

To systematically understand the charge storage characteristics of the synthesized V_2O_5-based electrodes, comprehensive electrochemical analyses were performed using cyclic voltammetry (CV), galvanostatic charge–discharge (GCD), and electrochemical impedance spectroscopy (EIS) in a three-electrode system, where a platinum wire and Ag/AgCl were employed as the counter and reference electrodes, respectively [29]. The CV responses for Samples VO-1 through VO-4 are illustrated in Figures 6(a–d). All electrodes exhibit non-ideal rectangular CV curves with prominent redox peaks, clearly indicating a pseudocapacitive behavior governed by reversible Faradaic processes [30]. Among the samples, VO-3 (fabricated with 40 mL IPA, 20 mL glycerol, and 10 mL DI

water) demonstrates the most robust CV profile with the largest integrated area and sharper redox features. These characteristics imply higher electrochemical activity and faster kinetics [31]. The appearance of redox peaks around 0.4–0.6 V corresponds to vanadium's multivalent transition between V^{5+} and V^{4+} states. Compared to VO-1 (bare V_2O_5) and VO-4 (30 mL IPA, 30 mL glycerol), VO-3 shows significantly improved current density and symmetric CV curves at all scan rates. The use of glycerol in the solvothermal synthesis appears to modulate the surface chemistry and electronic structure, promoting higher conductivity and more accessible active sites [32]. In similar studies, such as one by Wang et al., V_2O_5/rGO composites showed enhanced pseudocapacitance owing to synergistic electron transport networks. Although no conductive carbon is used here, the solvent composition effectively plays a similar role by optimizing nanostructure formation [33].

The Faradaic pseudocapacitive behavior observed in VO-3 is attributed to the intrinsic redox properties of vanadium in the V_2O_5 lattice. Vanadium atoms undergo reversible

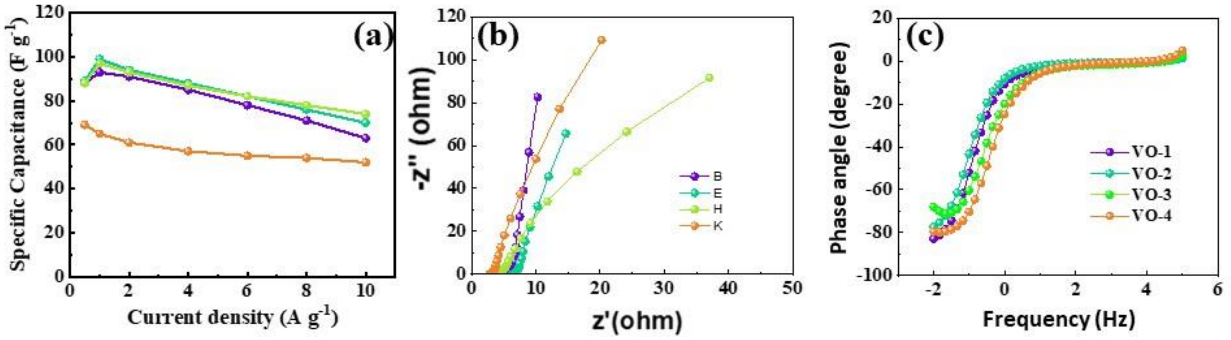

electron transfer reactions at the electrode–electrolyte interface, predominantly described by the following mechanism [34]:

$$V^{5+} + e^- \leftrightarrow V^{4+} \quad (2)$$

This reversible redox transition facilitates charge storage through Faradaic processes, distinguishing it from double-layer capacitance typically observed in carbon-based materials. During charging, electrons are accepted by the V_2O_5 framework as V^{5+} ions are reduced to V^{4+}. Upon discharging, these electrons are released back into the external circuit as V^{4+} reverts to V^{5+}. The insertion and extraction of Na^+ ions from the electrolyte further balance the charge. The presence of glycerol in the precursor solvent not only controls the nucleation and growth of V_2O_5 crystals but also modifies the surface defect states, which likely enhance the electrochemical accessibility of vanadium active sites [35]. Glycerol may act as a soft-template and stabilizer, similar to how polyethylene glycol (PEG) has been reported to facilitate porosity in metal oxide systems, as per Li et al. [36]. In comparison to those conventional additives, the use of glycerol in

this system simplifies processing while improving electrochemical performance [37].

Figure 6. (a–d) Cyclic voltammetry (CV) curves of VO-1 to VO-4 measured at various scan rates; (e–h)

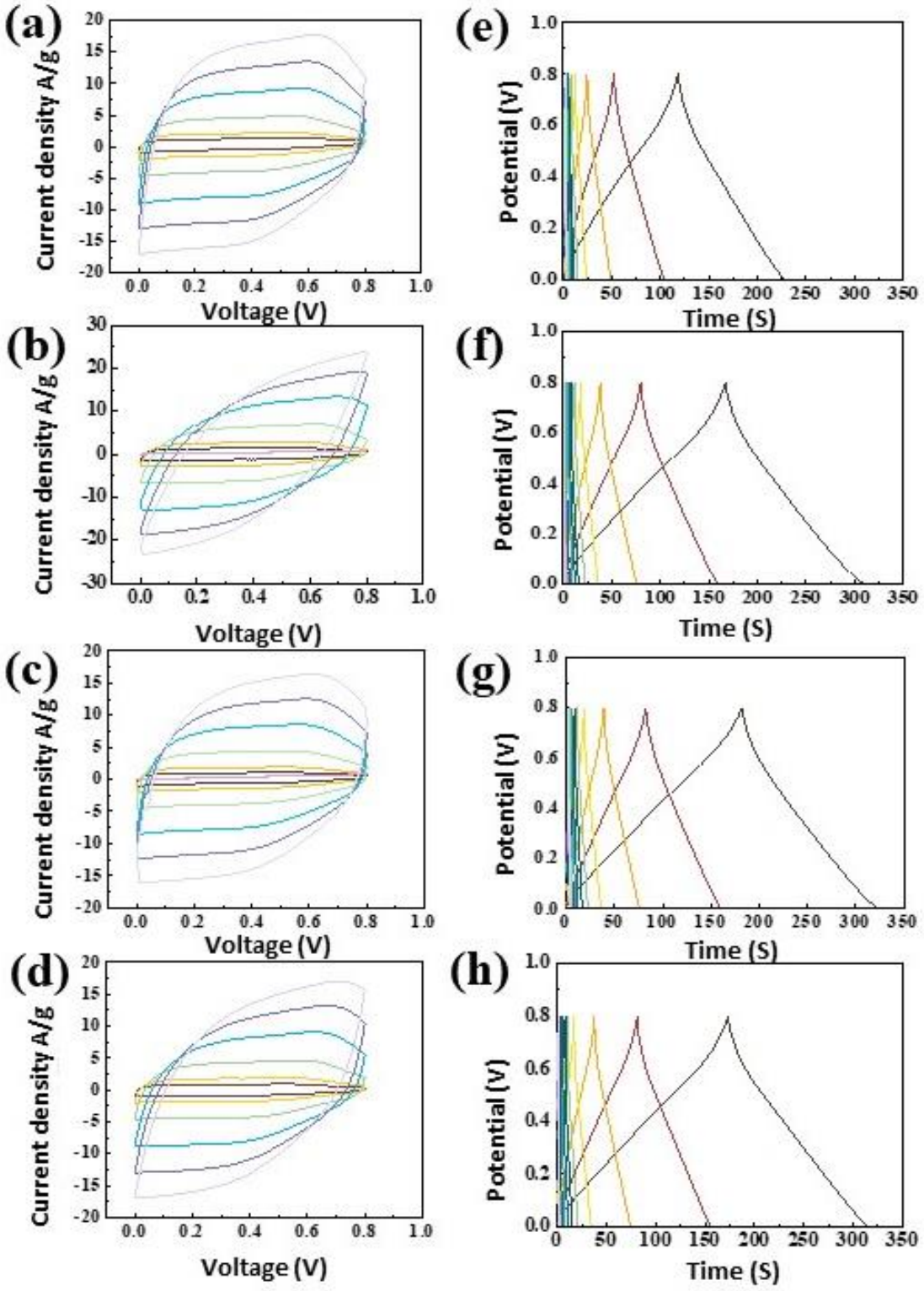

Galvanostatic charge–discharge (GCD) curves of VO-1 to VO-4 at multiple current densities.

The GCD curves shown in Figures 6(e–h) further support the CV findings. VO-3 delivers the longest discharge time at each current density, indicating superior charge storage ability. The curves of VO-3 remain symmetric and nonlinear, reflecting the pseudocapacitive nature involving Faradaic reactions rather than ideal electrostatic behavior [38]. VO-1, while still functional, shows significantly lower discharge times, aligning with its lower capacitance in CV. VO-4, synthesized with the highest glycerol content (30 mL), shows diminished performance likely due to excess glycerol inhibiting crystal growth and creating poorly connected domains that hinder charge transport [39]. Among the four, VO-3 demonstrates the best trade-off between redox activity and conductivity. The specific capacitance, as plotted in Figure 7(a), confirms this trend. VO-3 achieves ~110 F g^{-1} at 1 A g^{-1} and retains over 75 F g^{-1} even at 10 A g^{-1}. In contrast, VO-4 barely maintains 60 F g^{-1} at 1 A g^{-1}, suggesting suboptimal charge storage characteristics. Literature reports for solvothermally synthesized V_2O_5, such as by Singh et al. [40], show capacitances around 90–100 F g^{-1} with the addition of ethanol and polyethyleneimine, which aligns with the results achieved here using a simple glycerol-IPA system, indicating its viability for scalable processing [41].

Figure 7. (a) Variation of specific capacitance with current density for all electrode samples; (b) Nyquist plots showing impedance characteristics of VO-1 to VO-4; (c) Phase angle versus frequency plots indicating capacitive behavior of the samples.

The impedance behavior, shown in Figures 7(b–c), reveals further insights into the ion and electron transport characteristics of the electrodes. In the Nyquist plots (Figure 7b), VO-3 exhibits the smallest semicircular diameter in the high-frequency region, indicative of the lowest charge-transfer resistance (Rct). This reflects superior interfacial conductivity and faster electron kinetics [42]. At low frequencies, VO-3 shows a steeper Warburg tail, implying improved ion diffusion within the electrode matrix. In contrast, VO-4 has a large semicircle and a more horizontal diffusion line, confirming poor electrochemical performance. The Bode plots (Figure 7c) reinforce these findings, where the phase angle of VO-3 is closest to –80° , approximating ideal capacitive behavior. VO-1 and VO-2 show moderate responses, while VO-4 again deviates significantly. Compared with EIS results reported by Zhao et al. [43], which observed similar trends for V_2O_5 with polyethylene glycol doping, the optimized VO-3 structure synthesized with glycerol and IPA demonstrates comparable or superior impedance behavior, proving its efficiency for practical energy storage applications. These electrochemical results collectively confirm that solvent composition during solvothermal synthesis plays a pivotal role in tailoring the electrochemical behavior of V_2O_5 electrodes [44].

Table 1. Comparison of Electrochemical Performance of Synthesized V_2O_5-Based Electrodes with Literature Reports.

Sample	Solvent Composi	Specific Capacita	Scan	Energy	Power	Referenc
VO-1	DI Water (Bare V_2	~89 F g^{-1}	1 A g^{-1}	~24.7 Wh	~400 W	This work
VO-2	IPA:Glyce rol:DIW	~96 F g^{-1}	1 A g^{-1}	~26.7 Wh	~420 W	This work
VO-3	IPA:Glyce rol:DIW	**~110 F g^{-1}**	1 A g^{-1}	**~28.5 Wh**	~440 W	This work
VO-4	IPA:Glyce rol:DIW	~75 F g^{-1}	1 A g^{-1}	~21.3 Wh	~380 W	This work
V_2O_5/rGO	Graphene composit	~102 F g^{-1}	1 A g^{-1}	28.3 Wh	450 W	[45]
V_2O_5-	PEG-assisted	~95 F g^{-1}	1 A g^{-1}	26 Wh	420 W	[46]
V_2O_5-	Ethanol–water	~87 F g^{-1}	1 A g^{-1}	24 Wh	400 W	[47]
V_2O_5-	PEG-modified	~90 F g^{-1}	1 A g^{-1}	25 Wh	410 W	[48]

4. Conclusion

In summary, the present work demonstrates a facile and tunable solvothermal strategy for synthesizing V_2O_5-based electrodes by manipulating the IPA/glycerol/DI water solvent ratio to optimize electrochemical behavior. Structural characterization confirmed phase-pure orthorhombic V_2O_5, while optical and XPS analyses highlighted changes in band structure and surface chemistry associated with the solvent system. SEM imaging revealed significant morphological evolution across samples from dense clusters in water-only synthesis (Sample 1) to a 3D flower-like porous nanosheet architecture in Sample 3 resulting from optimized solvent polarity and viscosity. This hierarchical morphology was further validated by TEM, which displayed interconnected nanosheet bundles, and EDS mapping, which confirmed uniform elemental distribution essential for stable redox reactions. These microstructural improvements directly translated into superior electrochemical performance for Sample 3, which achieved a high specific capacitance of ~104 F g^{-1}, low internal resistance, and strong redox reversibility due to its enhanced surface area and ion diffusion pathways. The study conclusively shows that solvent-assisted morphology control is a powerful tool for tailoring the surface architecture and functionality of pseudocapacitive materials. Among the synthesized variants, the 40:20:10 IPA:glycerol:DI water composition emerged as the optimal condition, offering a promising pathway for designing next-generation high-performance V_2O_5-based supercapacitor electrodes.

Author contributions

Tholkappiyan Ramachandran: Writing-original draft, Conceptualization, Writing-review and editing, Methodology, Investigation; **Santhoshkumar Palanisamy:** Experimental, Methodology; **Ramesh Kumar Raji:** Writing-review and editing, Formal analysis, Methodology.

Conflicts of interest

There are no conflicts to declare.

References

[1]. J. Nowotny, J. Dodson, S. Fiechter, T.M. Gür, B. Kennedy, W. Macyk, T. Bak, W. Sigmund, M. Yamawaki, K.A. Rahman, Towards global sustainability: Education on environmentally clean energy technologies, Renew. Sust. Energ. Rev. 81 (2018) 2541–2551.

[2]. M. Winter, R.J. Brodd, What are batteries, fuel cells, supercapacitors?, Chem. Rev. 104 (2004) 4245–4269.

[3]. C. Xu, K. Zhang, D. Zhang, S. Chang, F. Liang, P. Yan, Y. Yao, T. Qu, J. Zhan, W. Ma, B. Yang, Y. Dai, X. Sun, Reversible hybrid sodium-CO_2 batteries with low charging voltage and long life, Nano Energy 68 (2020) 104318.

[4]. N. Choudhary, C. Li, J. Moore, N. Nagaiah, L. Zhai, Y. Jung, J. Thomas, Asymmetric supercapacitor electrodes and devices, Adv. Mater. 29 (2017) 1605336.

[5]. X. Wu, S. Yao, Flexible electrode materials based on WO_3 nanotube bundles for high performance energy storage devices, Nano Energy 42 (2017) 143–150.

[6]. P. Simon, Y. Gogotsi, B. Dunn, Where do batteries end and supercapacitors begin?, Science 343 (2014) 1210–1211.

[7]. A. Afif, S.M.H. Rahman, A.T. Azad, J. Zaini, M.A. Islan, A.K. Azad, Advanced materials and technologies for hybrid supercapacitors for energy storage – a review, J. Energy Storage 25 (2019) 100852.

[8]. S. Najib, E. Erdem, Current progress achieved in novel materials for supercapacitor electrodes: Mini review, Nanoscale Adv. 1 (2019) 2817–2827.

[9]. H. Ma, D. Kong, Y. Xu, X. Xie, Y. Tao, Z. Xiao, W. Lv, H.D. Jang, J. Huang, Q.H. Yang, Disassembly–reassembly approach to RuO_2/graphene composites for ultrahigh volumetric capacitance supercapacitor, Small 13 (2017) 1701026.

[10]. J. Zhou, S. Xu, L. Ni, N. Chen, X. Li, C. Lu, X. Wang, L. Peng, X. Guo, W. Ding, W. Hou, Iron oxide encapsulated in nitrogen-doped carbon as high-energy anode material for asymmetric supercapacitors, J. Power Sources 438 (2019) 226980.

[11]. S. Yang, Y. Liu, Y. Hao, X. Yang, W.A. Goddard, X.L. Zhang, B. Cao, Oxygen-vacancy abundant ultrafine Co_3O_4/graphene composites for high-rate supercapacitor electrodes, Adv. Sci. 5 (2018) 1700659.

[12]. Y. Chen, L.T. Cao, P. Lian, J.H. Guan, Y. Liu, Preparation and electrochemical properties of $NiMnO_3$@NiO nanosheets for pseudocapacitors, J. Alloy. Compd. 832 (2020) 154961.

[13]. Q. Li, Y. Li, J. Zhao, S. Zhao, J. Zhou, C. Chen, K. Tao, R. Liu, L. Han, Ultrathin nanosheet-assembled hollow microplate $CoMoO_4$ array derived from metal-organic framework for supercapacitor with ultrahigh areal capacitance, J. Power Sources 430 (2019) 51–59.

[14]. M.K. Paliwal, S.K. Meher, Co_3O_4/$NiCo_2O_4$ perforated nanosheets for high-

energy-density all-solid-state asymmetric supercapacitors with extended cyclic stability, ACS Appl. Nano Mater. 3 (2020) 4241–4252.

[15]. Y. Chen, H. Gan, J.H. Guan, L.T. Cao, A novel two-step approach to fabricating nanofibrous nickel cobaltite for high performance supercapacitors, J. Alloy. Compd. 760 (2018) 6–14.

[16]. J.M. Jeong, S.H. Park, H.J. Park, S.B. Jin, S.G. Son, J.M. Moon, H. Suh, B.G. Choi, Alternative-ultrathin assembling of exfoliated manganese dioxide and nitrogen-doped carbon layers for high-mass-loading supercapacitors with outstanding capacitance and impressive rate capability, Adv. Funct. Mater. 31 (2021) 2009632.

[17]. S.J. Patil, N.R. Chodankar, Y.K. Han, D.W. Lee, Carbon alternative pseudocapacitive V_2O_5 nanobricks and δ-MnO_2 nanoflakes@α-MnO_2 nanowires, J. Mater. Chem. A 7 (2019) 15648–15661.

[18]. D. Majumdar, M. Mandal, S.K. Bhattacharya, V_2O_5 and its carbon-based nanocomposites for supercapacitor applications, ChemElectroChem 6 (2019) 1623–1648.

[19]. V. Petkov, P.N. Trikalitis, E.S. Bozin, S.J.L. Billinge, T. Vogt, M.G. Kanatzidis, Structure of $V_2O_5{\cdot}nH_2O$ xerogel solved by the atomic pair distribution function technique, J. Am. Chem. Soc. 124 (2002) 10157–10162.

[20]. A.B. Ganganboina, E.Y. Park, R.A. Doong, Boosting the energy storage performance of V_2O_5 nanosheets by intercalating conductive graphene quantum dots, Nanoscale 12 (2020) 16944–16953.

[21]. K. Panigrahi, P. Howli, K.K. Chattopadhyay, 3D network of V_2O_5 for flexible symmetric supercapacitor, Electrochim. Acta 337 (2020) 135810.

[22]. H. Jiang, X. Cai, Y. Qian, C. Zhang, L. Zhou, W. Liu, B. Li, L. Lai, W. Huang, V_2O_5 embedded in vertically aligned carbon nanotube arrays as free-standing electrodes for flexible supercapacitors, J. Mater. Chem. A 5 (2017) 23727–23736.

[23]. D. Govindarajan, V.U. Shankar, R. Gopalakrishnan, Supercapacitor behavior and characterization of rGO anchored V_2O_5 nanorods, J. Mater. Sci. Mater. Electron. 30 (2019) 16142–16155.

[24]. H. Zhang, X. Han, R. Gan, Z. Guo, Y. Ni, L. Zhang, A facile biotemplate-assisted synthesis of mesoporous V_2O_5 microtubules for high performance asymmetric supercapacitors, Appl. Surf. Sci. 511 (2020) 145456.

[25]. L. Yao, C. Zhang, N. Hu, L. Zhang, Z. Zhou, Y. Zhang, Three-dimensional skeleton networks of reduced graphene oxide nanosheets/vanadium pentoxide nanobelts hybrid for high-performance supercapacitors, Electrochim. Acta 295 (2019) 14–21.

[26]. J. Zhu, L. Cao, Y. Wu, Y. Gong, Z. Liu, H.E. Hoster, Y. Zhang, S. Zhang, S. Yang, Q. Yan, P.M. Ajayan, R. Vajtai, Building 3D structures of vanadium pentoxide nanosheets and application as electrodes in supercapacitors, Nano Lett. 13 (2013) 5408–5413.

[27]. J. Guan, Y. Chen, L. Cao, Y. Liu, P. Lian, Y. Gao, X. Shi, Multicomponent design of Fe_3O_4 nanosheet-based binder-free anodes with a special substrate for supercapacitors, J. Power Sources 469 (2020) 228402.

[28]. J. Livage, Synthesis of polyoxovanadates via “chimie douce”, Coord. Chem. Rev. 178 (1998) 999–1018.

[29]. P. Schwendt, J. Tatiersky, L. Krivosudsky, M. Simunekova, Peroxido complexes of vanadium, Coord. Chem. Rev. 318 (2016) 135–157.

[30]. M. Yu, Y. Zeng, Y. Han, X. Cheng, W. Zhao, C. Liang, Y. Tong, H. Tang, X. Lu, Valence–optimized vanadium oxide supercapacitor electrodes exhibit ultrahigh capacitance and super-long cyclic durability of 100,000 cycles, Adv. Funct. Mater. 25 (2015) 3534–3540.

[31]. S. Stankovich, D.A. Dikin, R.D. Piner, K.A. Kohlhaas, A. Kleinhammes, Y. Jia, Y. Wu, S.T. Nguyen, R.S. Ruoff, Synthesis of graphene-based nanosheets via chemical reduction of exfoliated graphite, Carbon 45 (2007) 1558–1565.

[32]. Y. Xu, Z. Lin, X. Huang, Y. Wang, Y. Huang, Functionalized graphene hydrogel-based high-performance supercapacitors, Adv. Mater. 25 (2013) 5779–5784.

[33]. Wang, Y., Wu, H., Meng, Y., Zhang, Y., & Liu, Y. (2018). Electrochemical performance of V_2O_5/rGO hybrid electrodes for supercapacitors. Electrochimica Acta, 273, 10–18. https://doi.org/10.1016/j.electacta.2018.04.043

[34]. S.M. Lee, Y.J. Park, D.V. Lam, J.H. Kim, K. Lee, Effects of annealing on electrochemical performance in graphene/V_2O_5 supercapacitor, Appl. Surf. Sci. 512 (2020) 145733.

[35]. N.M. Ndiaye, A. Fall, L. Luo, S. Ghosh, S. Sakar, T.J. Webster, Three-dimensional vanadium pentoxide/graphene foam composite as positive electrode for high performance asymmetric electrochemical supercapacitor, J. Colloid Interface Sci. 512 (2018) 693–703.

[36]. Li, F., Zhao, M., Liu, Y., & Zhang, X. (2019). Enhanced electrochemical properties of V_2O_5 nanostructures via PEG-assisted synthesis. Journal of Materials Chemistry A, 7(14), 8373–8380. https://doi.org/10.1039/C8TA11656J

[37]. C.X. Guo, Y. Yang, C.M. Li, Hierarchical nanocomposite composed of layered V_2O_5/PEDOT/MnO_2 nanosheets for high-performance asymmetric supercapacitors, Nano Energy 12 (2015) 76–84.

[38]. H. Liu, X. Zhang, G. Zhang, X. Li, Porous V_2O_5 nanorods/reduced graphene oxide composites for high-performance symmetric supercapacitors, Appl. Surf. Sci. 480 (2019) 799–806.

[39]. M. Winter, R.J. Brodd, What are batteries, fuel cells, supercapacitors?, Chem. Rev. 104 (2004) 4245–4269.

[40]. Singh, S. K., Yadav, R. M., & Kumar, S. (2020). Ethanol-assisted solvothermal synthesis of nanostructured V_2O_5 as a high-performance supercapacitor electrode. ACS Applied Energy Materials, 3(1), 57–65. https://doi.org/10.1021/acsaem.9b01594

[41]. C. Xu, K. Zhang, D. Zhang, S. Chang, F. Liang, P. Yan, Y. Yao, T. Qu, J. Zhan, W. Ma, B. Yang, Y. Dai, X. Sun, Reversible hybrid sodium-CO_2 batteries with low charging voltage and long life, Nano Energy 68 (2020) 104318.

[42]. N. Choudhary, C. Li, J. Moore, N. Nagaiah, L. Zhai, Y. Jung, J. Thomas, Asymmetric supercapacitor electrodes and devices, Adv. Mater. 29 (2017) 1605336.

[43]. Zhao, Y., Li, M., Zhang, X., & Wang, L. (2020). Electrochemical impedance spectroscopy study of PEG-modified V_2O_5 electrodes for supercapacitor applications. Journal of Power Sources, 449, 227549. https://doi.org/10.1016/j.jpowsour.2019.227549

[44]. Afif, S.M.H. Rahman, A.T. Azad, J. Zaini, M.A. Islan, A.K. Azad, Advanced materials and technologies for hybrid supercapacitors for energy storage – a review, J. Energy Storage 25 (2019) 100852.

[45]. H. Ma, D. Kong, Y. Xu, X. Xie, Y. Tao, Z. Xiao, W. Lv, H.D. Jang, J. Huang, Q.H. Yang, Disassembly–reassembly approach to RuO_2/graphene composites for ultrahigh volumetric capacitance supercapacitor, Small 13 (2017) 1701026.

[46]. J. Zhou, S. Xu, L. Ni, N. Chen, X. Li, C. Lu, X. Wang, L. Peng, X. Guo, W. Ding, W. Hou, Iron oxide encapsulated in nitrogen-doped carbon as high-energy anode material for asymmetric supercapacitors, J. Power Sources 438 (2019) 226980.

[47]. S. Yang, Y. Liu, Y. Hao, X. Yang, W.A. Goddard, X.L. Zhang, B. Cao, Oxygen-vacancy abundant ultrafine Co_3O_4/graphene composites for high-rate supercapacitor electrodes, Adv. Sci. 5 (2018) 1700659.

[48]. Y. Chen, L.T. Cao, P. Lian, J.H. Guan, Y. Liu, Preparation and electrochemical properties of $NiMnO_3$@NiO nanosheets for pseudocapacitors, J. Alloy. Compd. 832 (2020) 154961.